Journal of Environmental Chemical Engineering 9 (2021) 106217

Contents lists available at ScienceDirect

Journal of Environmental Chemical Engineering

journal homepage: www.elsevier.com/locate/jece

Experimental and CFD evaluation of ozone efficacy against coronavirus and enteric virus contamination on public transport surfaces

Irene Falcó [a], Walter Randazzo [a], Gloria Sánchez [a], Jose Vilarroig [b], Javier Climent [b], Sergio Chiva [c], A. Chica [d], J. Navarro-Laboulais [e,*]

[a] Department of Preservation and Food Safety Technologies, Institute of Agrochemistry and Food Technology, IATA-CSIC, Av. Agustín Escardino 7, Paterna, 46980 Valencia, Spain
[b] Hydrodynamic and Environmental Services, Av. del Mar, 53, 12003 Castellón, Spain
[c] Universitat Jaume I, Department of Mechanical Engineering and Construction, Av. Vicent Sos Baynat, s/n, 12071 Castellón, Spain
[d] Instituto de Tecnología Química, Universitat Politècnica de València-Consejo Superior de Investigaciones Científicas, Avd. de Los Naranjos s/n, 46022 Valencia, Spain
[e] Department of Chemical and Nuclear Engineering, Universitat Politècnica de València, Camino de Vera s/n, 46022 Valencia, Spain

ARTICLE INFO

Editor: Dr. G. Palmisano

Keywords:
Ozonation
Disinfection
SARS-CoV-2
Coronavirus
Enteric virus
CFD public transport

ABSTRACT

The limited information about the routes of the transmission of SARS-CoV-2 within the ongoing pandemic scenario mobilized the administration, industry and academy to develop sanitation and disinfection systems for public and private spaces. Ozone has been proposed as an effective disinfection method against enveloped and non-enveloped viruses, including viruses with similar morphology to SARS-CoV-2. Due to this efficacy, numerous gaseous and aqueous phase ozone applications have emerged potentially to inhibit virus persistence in aerosols, surfaces, and water. In this work, a numerical model, a RANS CFD model for ozone dispersion inside tram and underground coach has been developed including the chemical self-decomposition and surface reactions of the ozone. The CFD model has been developed for a real tram coach of 28.6 × 2.4 × 2.2 m (L × W × H) using 1.76 million nodes and the Menter's shear stress transport turbulence model. The model predicts the O_3 concentration needed to meet disinfection criteria and the fluid dynamics inside the public transport coach. The effectiveness of the system has been validated with laboratory and field tests in real full-scale coach using porcine epidemic diarrhea virus (PEDV) and murine norovirus (MNV-1) as SARS-CoV-2 and human norovirus surrogates, respectively. Lab-scale experiments on plastic surfaces demonstrated O_3 disinfection (100 ppm, 95% RH, 25 min) inactivate > 99.8% MNV-1 and PEDV. Additionally, field tests in real full-scale coach demostrate the efficacy of the system as > 98.6% of infectious MNV-1 and > 96.3% PEDV were inactivated.

1. Introduction

The emergence of severe acute respiratory syndrome coronavirus-2 (SARS-CoV-2) has become a global health concern and the primary intervention being used worldwide has being the control of infections by preventing viral spread. The major SARS-CoV-2 transmission routes are aerosols and respiratory droplets loaded with the virus [1,2]. However, recent investigations reported the presence of SARS-CoV-2 RNA in public surfaces, including those of metropolitan public transports such as underground and buses [3,4]. These findings indicated not only the contamination of surfaces but also the circulation of infected patients finally pointing out to public transport as potential hot-spots for infection. Thus, rigorous hygiene measures are demanded to prevent viral spread via contaminated air, hands or surfaces [5–7].

Among others, ozone (O_3) is an extreme oxidizer that significantly affects the viability of microorganisms, including viruses. The strong oxidizing potential of the ozone (2.07 V vs Normal Hydrogen Electrode) reacts with the glycoproteins, glycolipids, purine and pyrimidine bases of DNA, and sulfhydryl groups which degrades the lipid cell structures and makes inviable their function [8]. Many viruses require membrane glycoproteins to be in the reduced form rather than oxidized for membrane fusion and successful host cells penetration. Coronaviruses have abundant cysteine and tryptophan in their spike and envelope proteins that are highly vulnerable to oxidation with ozone or other oxidizing treatments [9–12]. The first use of ozone was the drinking water disinfection with early full-scale treatment plants since the beginning of

* Corresponding author.
E-mail address: jnavarla@iqn.upv.es (J. Navarro-Laboulais).

https://doi.org/10.1016/j.jece.2021.106217
Received 18 June 2021; Received in revised form 31 July 2021; Accepted 13 August 2021
Available online 17 August 2021

XX century [13]. Although there is a vast literature on the ozone concentration and exposure times needed for bacterial and protozoan inactivation in wastewater treatment, scarce data are available for controlling viral contamination [14]. Previous data showed that both murine coronavirus and SARS-CoV-1 [15,16] are readily inactivated by O_3 treatment especially when combined with high relative humidity (RH) and this outcome has been conveyed to SARS-CoV-2 based on a recent computational analysis [17]. Recently the virucidal efficacy of the ozone has been reviewed considering the best environmental condition, i.e. temperature and humidity, the ozone concentration and contact times, for a broad number of independent viruses [18]. The ozone could be an efficient potential disinfectant against SARS-CoV-2 because the lipid envelope can be readily degraded by ozone [14,18]. However, robust experimental evidence on the efficacy of this disinfectant under realistic conditions is still lacking finally limiting the establishment of well-defined decontamination procedures that is a paramount priority.

The ozone gas is soluble in respiratory droplets and its maximum concentration in these droplets is a function of the gas concentration [19]. Even for low concentrations, the ozone can be effective on viruses suspended in aerosols and then, it can be useful for decontamination of public indoor spaces such as hospitals and other workplaces facilities, and public transport systems where there is a lack of proper ventilation removal design. The use of ozone in occupied indoor spaces is limited because this gas is associated with respiratory issues and demonstrated decrements in the pulmonary function when adults are exposed for 6.6 h at 0.08 ppm (160 μg/m^3) of ozone, 2.0 h at 0.12 ppm (240 μg/m^3) and 1.0 h at 0.25 ppm (500 μg/m^3) [20]. Thus, disinfection strategies in indoor environments using higher ozone concentrations must be set up only when these spaces remain unoccupied. These strategies imply an injection of a high ozone dose in the environment to be decontaminated, a waiting time to ensure virus inactivation and an additional time frame to ensure the ozone–self-decomposition to oxygen below the health risk exposure concentration.

The ozone-indoor-disinfection strategy should be properly designed because there are additional factors to be considered such as (i) the materials degradation, (ii) the generation of by products, (iii) the residual ozone and (iv) the inactivation of viruses either present in air and on surfaces. Moreover, as a well-mixed assumption might not be appropriate due to the spatial variations in the concentrations of chemicals within the domain [21,22], Computational Fluid Dynamics (CFD) has been used as support tool for the ozone dispersion in complex indoor full-scale domains [23], including ozone surface reactions and its decomposition [24]. These contributions can be determined for various materials in real environments to be implemented in the CFD model [25]. Because the strong oxidizing potential of the ozone, the gas can react with solid surfaces and synthetic materials commonly present in indoor environments, such as wood, rubber, fabrics, paints, linoleum, carpets, etc. finally giving a large set of complex by-products [26]. Thus, as longer the ozone exposition as more esthetic, mechanical and chemical properties of the materials will change. Related with this gas-solid reactions, the ozone can generate a variety of disinfection-by-products (DBPs) which can lead the formation of health-risk substances such as aldehydes, ketones, peroxides and carboxylic acids [23,27–29]. The rate of formation and fate of these substances is a function of several factors such as the ozone concentration, temperature, humidity and pressure. Thus, the ozone exposure CT (concentration-time factor) should be high enough to inactivate the microorganisms but minimize the DBPs. Finally, after the disinfection, some residual ozone can remain on the air with concentrations above the permissible exposure limits recommended by institutions like World Health Organization, US Environmental Protection Agency or European Union Regulators. The half-time of the ozone self-decomposition rate is above 2–10 h in bulk air depending the ambient conditions or even days in dark conditions [30–34]. In order to reduce this residual ozone in a reasonable lapse of time, it is necessary the use of catalysts and catalytic devices, which reduces the self-decomposition half-times in few minutes. The catalysts used for ozone decomposition are mainly based on MnO_2 doped with other metal oxides such as CuO or NiO [35] but other catalysts based on carbonaceous materials, i.e. activated carbon, graphite, carbon fibers, have also been proposed [36,37]. These catalysts are effective for ozone decomposition and cheap materials but the effectiveness reduction caused by humidity on MnO_2 or its inactivation by surface oxygenated compounds formation are known issues which restrain the use and capacity of these materials.

A final aspect that should be considered in ozone-disinfection strategies against SARS-CoV-2 is the effect of the indoor surfaces in relation with the survival of the virus and its relevance in the transmission of the disease. Despite the inherent methodological difficulties to evaluate the survival of infectious viruses on surfaces, the transmission of the disease by direct contact of contaminated surfaces is controversial [38]. Although the aerial way is accepted as the main transmission route of SARS-CoV-2, the transmission of the disease by contaminated surfaces cannot be discarded, mainly in healthcare environments [39]. Regardless the contribution of contaminated surfaces on the virus transmission, there are robust experimental evidences that the whole-room disinfection systems based on disinfectant atomized aerosols or gases like the ozone together conventional cleaning procedures reduces significantly microbial contamination of surfaces [15,40].

The purpose of this work was to provide experimental evidences on the virucidal performance of ozone in public transport systems using a disinfection facility, which injects an ozone boost in the unoccupied space of the transport unit. The experiments were carried out in real scale tram and underground coach but the procedure can be extended to other vehicles like coaches and airplanes and other building indoor spaces. The ozone concentration distribution inside the coach were determined by computational fluid dynamics tools (CFD) coupled with ozone self-decomposition reaction kinetics and ozone-reactive surfaces. After the validation of the numerical model, the virucidal performance of the ozone at real scale were determined using *in-vitro* tests with SARS-CoV-2 and human norovirus surrogates.

2. Materials and methods

2.1. Numerical simulations

A three-dimensional CFD model was performed to evaluate aerodynamics in detail in the real scale of both types of public transport coaches. Once the fluid flow behavior was validated, the dispersion of a pulse of ozone was studied through the analysis of the concentration distribution in the domains. Both 3D geometries were performed using the Space Claim, and the simulations were run in ANSYS® Release 19.2 CFX package [41]. Full description of the equations, methods, computational framework and 3D meshing procedure and structure used on CFD calculations are described in the Supplementary material of the paper.

The resulting meshes for the simulations were hexahedral dominant with about 1.76 million nodes. The guidelines detailed in CFX Best Practices Guide [41] or Numerical Accuracy were considered, mesh quality parameters (orthogonal quality of 9.9676, and skewness of 0.1753) were checked for the defined mesh.

A gas single-phase model approach was defined at 25 °C. The Shear Stress Transport (SST) developed by Menter was selected as the turbulence model [42]. This two-equation eddy-viscosity turbulence model uses the k-ω model near the walls and the k-ε in the remote areas. It is appropriate for this simulation since the aim is to precisely examine the boundary layer for which a fine near-wall mesh has been produced. The automatic near-wall treatment was selected. It allows a consistent transition between regions with coarse meshes, where the viscous sublayer is modeled using the scalable wall functions developed by ANSYS, to regions with fine meshes. For the SST model, it is necessary to use a mesh with a y+ below 2, so that the model is able to determine and use

the functions of the wall or not.

The approximate dimensions of the models were 28.6 m × 2.4 m × 2.2 m for the tram coach, and 26.7 m × 2.3 m × 2.18 m for the underground, which corresponded to half wagon. The distribution of the seats can be highlighted among the internal elements within the domains (Fig. 1). An external pipe of 600 mm was set in parallel to force the recirculation of the air and the ozone through the domains. The SDA-200 industrial fan was implemented as submodel inside the pipe, and it was previously calibrated to determine the volumetric momentum source term of 1269 kg/m^2 s^2 which corresponded to 12 m/s air velocity inside the pipe.

A comprehensive analysis of the air motion inside the system was carried out and validated experimentally. Once the fluid dynamics was evaluated, the ozone was introduced to determine its concentration distribution in the system. Thus, once the fluid dynamics was steady, a total mass of 30 g was injected through a pulse of 5 min.

2.1.1. Implementation of the ozone kinetics

The ozone was implemented as an additional scalar field by means of a transport equation:

$$\frac{\partial}{\partial t}(\rho.\varphi_i) + \nabla.(\rho.U.\varphi_i) = \nabla.\left[\left(\rho.D_{\Phi}. + \frac{\mu_t}{Sc_t}\right)\nabla\varphi_i\right] + S_{\varphi_i} \quad (1)$$

where U is the fluid velocity (m s^{-1}), ρ is the mixture density (kg m^{-3}), Φ is the concentration of the i variable (kg m^{-3}), $\varphi = \Phi/\rho$ is the conserved quantity of i variable per unit mass of fluid, Sct is the Turbulence Schmidt number, μ_t is the turbulence viscosity term in Pa s, D_{Φ} is the kinematic diffusivity (m^2 s^{-1}) and S_{φ_i} is a volumetric source term (kg m^{-3} s^{-1}) that embeds the chemical reactions.

To solve correctly the ozone consumption inside the domains, it is necessary to have an appropriate model to calculate the rate of ozone reaction (removal) on the surfaces of the system and that in turn can be implemented in the CFD model. For this, an analytical model consisting of algebraic equations has been used that allow quantifying the speed of ozone elimination due to two main mechanisms [23]: (i) fluid motion and ozone diffusion (molecular transport of ozone) around surfaces; (ii) chemical reactions of ozone on surfaces.

The ozone surface removal on material surfaces depends on the local ozone concentration adjacent to the surface. The main limitation of CFD modeling to calculate the sink surface deposition flux correctly is that extremely fine meshes near the surfaces are required, values of 10^{-8} for the distance from the surface to the first calculation node. Because of this, the model proposed by Sørensen and Weschler was implemented in the CFD model [21]. It allows the calculation for larger meshes as long as a boundary layer flow prevails over most of the surface area, which is controlled by the distance to the first node, Δy_1, following the equation:

$$J_s = -\frac{\gamma\frac{v}{4}}{1 + \left(\frac{\gamma v}{4}\Big/ D_m\right)(\Delta y_1)} \cdot C(\Delta y_1) \quad (2)$$

where γ is the reaction probability (non-dimensional), defined as the fraction of collisions of ozone molecules at the surface that result in irreversible uptake, v is the Boltzmann velocity for the chemical species which has a value of 3.6 10^4 cm s^{-1} for ozone at 293 K, $C(\Delta y)$ (kg/m3) is the ozone concentration at $\Delta y = 2\lambda/3$, where λ mean the molecular free path (6.5 × 10^{-8} m), D_m is the binary diffusion coefficient of the chemical species in air (m^2/s). Therefore, knowing the distance to the first node (Δy_1) and the surface material (γ), the ozone removal on the surfaces can be calculated by CFD simulation.

It is important to highlight that the magnitude of the γ parameter can be quantified [43] and depends on the specific material, being a flow-independent parameter [27]. Separate tests should be performed to properly calibrate each of the materials. In this case, the different materials that make up the coaches: glass, metal, synthetic material and carpet, have been taken as average values previously reported [23,27].

2.1.2. Ozone self-decomposition reaction rate model

The ozone self-decomposes spontaneously given molecular oxygen. The rate at which this reaction takes place is relevant for the evaluation of the ozone concentration distribution after the injection of the gas in the tram coach. The first self-decomposition models were based on chemical mechanism initiated by third-body reactions [30–32,44]. This model predicts reaction half-times at ambient temperature of several orders of magnitude higher the observed ones. Then, instead this simplified model, a detailed chemical model considering the chemical and photochemical reactions of the ozone with all the chemicals presents in the air has been considered in this work.

The chemical reactions and values of the reaction rate constants for the ozone chemistry are compiled by international institutions devoted to atmospheric chemistry and such as Jet Propulsion Laboratory (NASA-JPL) [45], IUPAC Task Group on Atmospheric Chemical Kinetic Data Evaluation [46] and the kinetics database of the National Institute of Standards and Technology [47]. From these databases can be extracted a basic set of ozone chemical reactions which can be modified by other chemical reactions involving volatile organic compounds or nitrogen oxides leading to urban air or indoor detailed chemical models.

The California Statewide Air Pollution Research Center (SAPRC) Model [48] is a complete set of self-consistent chemical reactions, continuously updated since 1990, and used for air quality simulation models. In this study, the SAPRC-18 Model was used for the simulation of ozone self-decomposition and for the derivation of a simplified rate equation to be implemented on the CFD code instead using the complete chemical mechanism, which overloads the calculations. For this purpose, only the inorganic part of the SAPRC-18 Model without the sulfur reactions contribution has been considered (Table 1). This is a set of 45 chemical reactions involving 17 chemical species with the photochemical reactions of NO_x and O_3. The simulation of the ozone decomposition model was carried out using the kinetic preprocessor program, KPP, [49,50] generating the Matlab code to solve the chemical dynamics of the system.

The ozone self-decomposition rate equation has been derived analyzing the ozone concentration profiles under different initial conditions. The effect of the light and the relative humidity have considered on ozone decomposition rate. The SAPRC-18 Model provides the photochemical rate constants as a function of the relative intensity of the

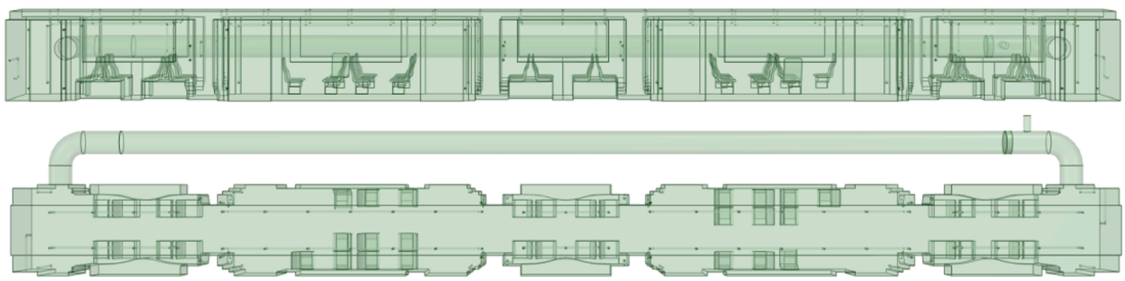

Fig. 1. 3D domain of the tram coach.

Table 1
Simplified ozone self-decomposition model based on inorganic part of SAPRC-18 Model. The reaction rate constants are evaluated at 298.15 K.

# Rxn	Reaction	k (cm^3 $molec^{-1}$ s^{-1})
{1}	$NO_2 + h\nu \rightarrow NO + O(^3P)$	1.204E-02
{2}	$O(^3P) + O_2 + M = O_3$	5.904E-34
{3}	$O(^3P) + O3 = Products$	7.960E-15
{4}	$O(^3P) + NO = NO_2$	1.664E-12
{5}	$O(^3P) + NO_2 = NO$	1.032E-11
{6}	$O(^3P) + NO_2 = NO_3$	3.284E-12
{7}	$O_3 + NO = NO_2$	1.955E-14
{8}	$O_3 + NO_2 = NO_3$	3.226E-17
{9}	$NO + NO_3 = 2NO_2$	2.654E-11
{10}	$NO + NO + O_2 = 2NO_2$	1.954E-38
{11}	$NO_2 + NO_3 = N_2O_5$	1.241E-12
{12}	$N_2O_5 = NO_2 + NO_3$	4.459E-02
{13}	$N_2O_5 + H_2O = 2HNO_3$	0.000E+00
{14}	$N_2O_5 + H_2O + H_2O = 2HNO_3$	0.000E+00
{15}	$NO_2 + NO_3 = NO + NO_2$	6.560E-16
{16}	$NO_3 + h\nu = NO$	3.182E-02
{17}	$NO_3 + h\nu = NO2 + O(^3P)$	2.567E-01
{18}	$O_3 + h\nu = O(^1D)$	5.095E-05
{19}	$O_3 + h\nu = O(^3P)$	6.107E-04
{20}	$O(^1D) + H_2O = 2OH$	1.994E-10
{21}	$O(^1D) + M = O(^3P)$	3.690E-11
{22}	$OH + NO = HONO$	7.408E-12
{23}	$HONO + h\nu = OH + NO$	1.900E-03
{24}	$OH + HONO = NO_2$	4.863E-12
{25}	$OH + NO_2 = HNO_3$	9.892E-12
{26}	$OH + NO_3 = HO_2 + NO_2$	2.200E-11
{27}	$OH + HNO_3 = NO_3$	1.543E-13
{28}	$HNO_3 + h\nu = OH + NO_2$	9.003E-07
{29}	$OH + O_3 = HO_2$	7.253E-14
{30}	$HO_2 + NO = OH + NO_2$	8.166E-12
{31}	$HO_2 + NO = HNO_3$	4.332E-14
{32}	$HO_2 + NO + H_2O = HNO_3$	2.351E-31
{33}	$HO_2 + NO_2 = HNO_4$	7.503E-13
{34}	$HNO_4 = HO_2 + NO_2$	6.200E-02
{35}	$HNO_4 + h\nu = 0.8\ (HO_2 + NO_2) + 0.2\ (OH + NO_3)$	9.033E-06
{36}	$HNO_4 + OH = NO_2$	4.653E-12
{37}	$HO_2 + O_3 = OH$	1.931E-15
{38}	$HO_2 + HO_2 = HO_2H$	2.538E-12
{39}	$HO_2 + HO_2 + H_2O = HO_2H$	5.712E-30
{40}	$NO_3 + HO_2 = OH + NO_2$	3.500E-12
{41}	$NO_3 + NO_3 = 2NO_2$	2.285E-16
{42}	$HO_2H + h\nu = 2OH$	9.397E-06
{43}	$HO_2H + OH = HO_2$	1.800E-12
{44}	$OH + HO_2 = Products$	1.111E-10
{45}	$O_3 + O_2 = O_2 + O_2 + O(3P)$	2.00E-26

irradiating light of the sun, then it is possible to trace the evolution of the ozone concentration with this intensity (Fig. 3a). Inside the tram and underground coaches the light intensity is lower the maximum solar light attainable in open air, and then for the simulations, the worst-case scenario regarding the ozone decomposition has been considered. The decomposition rate is maximum for high relative light intensity then for simulation purposes it will be considered SUN = 1 and any other situation in real system will lead to a slower ozone decomposition.

The ambient humidity also has an effect of ozone self-decomposition and as is shown in Fig. 3b. For higher water content, higher is the ozone self-decomposition rate. The relative humidity (HR) is defined as the ratio of the actual water pressure (P_{H_2O}) and the saturation water pressure ($P^{\bullet}_{H_2O}$):

$$HR = \frac{P_{H_2O}}{P^{\bullet}_{H_2O}} \tag{3}$$

The saturation water pressure was calculated from Buck's equation [51]:

$$P^{\bullet}_{H_2O}(\mathrm{Pa}) = 611.21 \cdot \exp\left[\left(18.678 - \frac{t}{234.5}\right)\left(\frac{t}{257.14 + t}\right)\right] \tag{4}$$

Known the partial pressure of water it is possible estimate its initial concentration (in ppm) for each simulation.

All the simulations of the ozone self-decomposition with T = 298.15 K, $0 \leq HR \leq 100\%$ and $0 \leq SUN \leq 1.0$ give an apparent reaction order of 1.44 for the ozone. This reaction order has been checked for all simulations and ozone conversions higher than 70%. In conclusion, using all the simulation data at ambient temperature with the maximum light and humidity simulated intervals, the following ozone self-decomposition reaction rate can be derived:

$$-r_{O_3}\left(\frac{ppm}{s}\right) = 3.886 \cdot 10^{-6} \cdot HR^{0.417} \cdot SUN^{0.624} \cdot [O_3]^{1.44} \tag{5}$$

where the ozone concentration is expressed in ppm, $0 \leq SUN \leq 1.0$ and $0 \leq HR \leq 100\%$. The rate coefficient units are $ppm^{-0.44}$ s^{-1} to be consistent with the rate units. This rate equation is implemented on CFD code for the estimation of ozone decomposition on the train ambient after the gas injection. This equation avoids the use of the detailed chemical model (Table 1) which reduces considerably the computational cost of the fluid simulations. The simulations of ozone decomposition were performed in absence of nitrogen oxides, which react fast with the ozone.

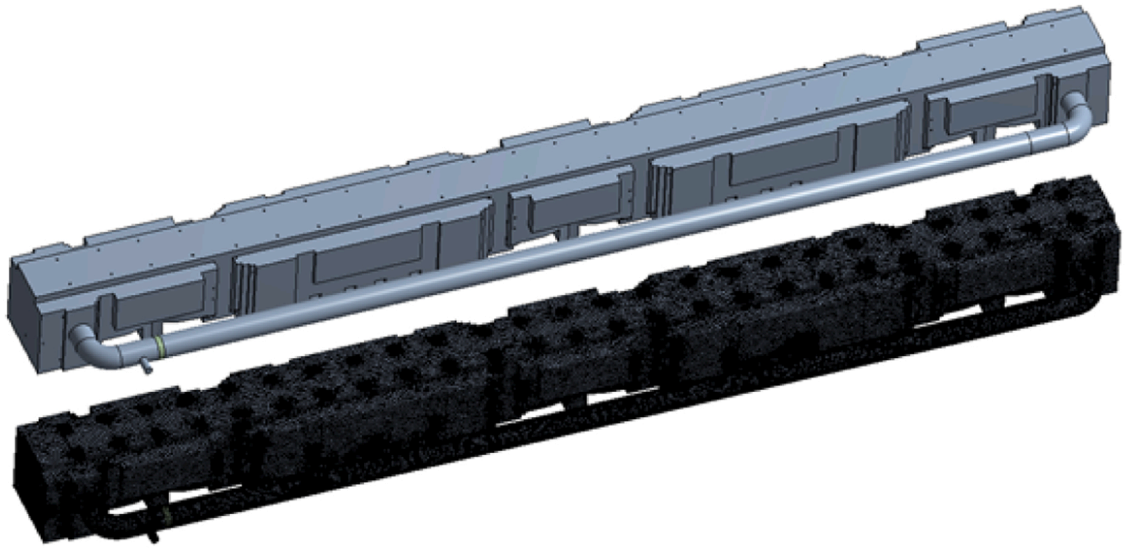

Fig. 2. 3D domain external view and the mesh of the tram coach.

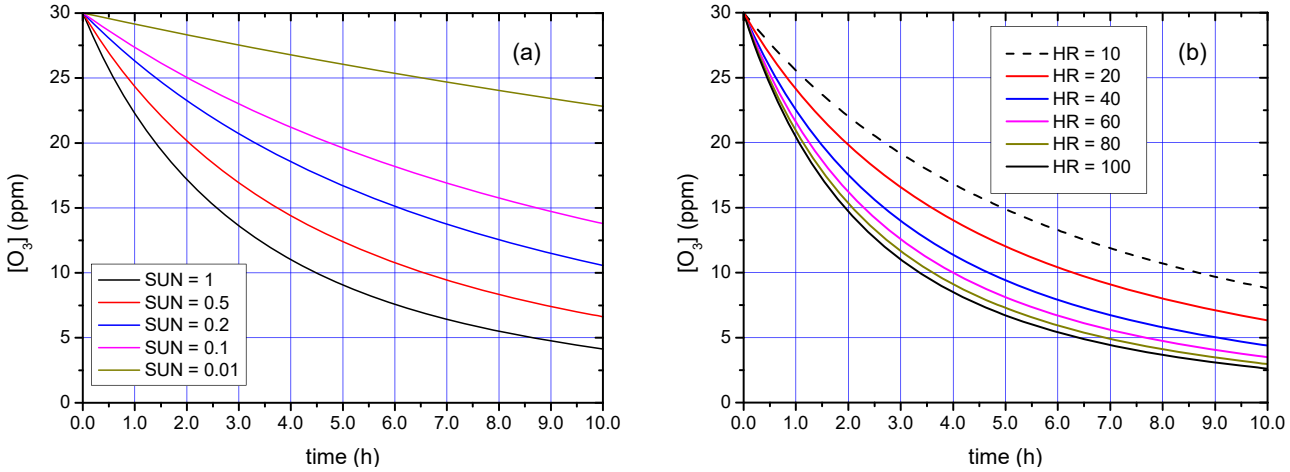

Fig. 3. Ozone self-decomposition for different relative Sun light (a) and different relative humidity (b). For the simulations $[O_3]_0 = 30$ ppm; T = 298.15 K; PT = 1.0 atm; $y_{O2} = 0.2095$; $y_{N2} = 0.79$. The plot in (a) has been obtained with HR = 65% and the plot in (b) considering SUN = 1. The plots are the simulation of the reaction mechanism shown in Table 1.

2.2. Experimental set-up

2.2.1. Underground and tram coaches

An underground and a tram coach were used as public transport reference domains to develop three-dimensional CFD models and to run field experiments to validate both CFD models and viral inactivation kinetics. Specifically, the S-3900 model produced by GEC-ALSTHOM and the S-4200 model produced by Bombardier Transportation S.A. both owned by "Ferrocarrils de la Generalitat Valenciana" (FGV, Spain) were used as underground and tram public transport representative models, respectively.

2.2.2. Ozonation system

The experimental installation, the SDA-200-50 equipment produced by LIC–VARESER (Spain), consisted in a closed loop conduction of 600 mm of diameter, parallel to the tram coach connecting their opposite end doors and where the ozone was continuously recirculated (Figs. 1 and 2). The ozone was generated with Fujian Allied Power Mod HW-OS-50 ozone generation able to produce 50 g-O_3/h fed by PSA oxygen. The ozone was generated at 1 bar in a rate of 5 L/min. The ozone was accumulated in a 500 L pressure tank just before the injection in order to reduce the transfer time of the ozone to the recirculation loop. The maximum attained pressure is 2 bar to avoid ozone decomposition. The ozone is accumulated in 1 h cycles and injected in less than 5 min.

The produced ozone concentration is measured with API Mod. 452 Ozone meter with UV detection able to measure under 500 g-O_3/N m^3 with pressure and temperature compensation. The ozone concentration inside the tramway cabin were measured with ECO-Sensors Mod. OS-6 solid state ozone detector able to measure under 50 ppm.

The average concentration of the ozone attained in the coaches was in the order of 55 ppm of ozone with application times in the order of 20–30 min.

2.2.3. Viruses used in the study

To evaluate the viral inactivation of ozone treatments for the surface disinfection of public transport and tram coaches we selected murine norovirus (MNV), a norovirus surrogate, and porcine epidemic diarrhea virus (PEDV) as models for non-enveloped and enveloped viruses, respectively. PEDV was selected as SARS-CoV-2 surrogate as biosafety laboratories level 3 are required for SARS-CoV-2 cell-culture, which are of limited access. The cytopathogenic PEDV strain CV777, an enveloped virus member of the *Coronaviridae* family, and the MNV-1 strain (a non-enveloped virus) was propagated and assayed in Vero (kindly provided by Prof. A. Carvajal, University of Leon, Spain) and RAW 264.7 cells (kindly provided by Prof. H.W. Virgin, Washington University School of Medicine, USA), respectively. Semi-purified stocks were subsequently produced from the same cells by centrifugation of infected cell lysates at 660 × *g* for 30 min. Infectious viruses were enumerated by determining the 50% tissue culture infectious dose ($TCID_{50}$/mL) with eight wells per dilution and 20 μL of inoculum per well [52].

2.2.4. Viral inactivation kinetics in lab-scale experiments

Initially, the virucidal activity of ozone was assessed at lab-scale on hard (polypropylene plastic) and porous surfaces (upholstery) by adapting the ISO 21702:2019 (Measurement of antiviral activity on plastics and other non-porous surfaces) and ISO 18184:2019 (Determination of antiviral activity of textile products). Briefly, 100 μL suspensions of PEDV and MNV were seeded onto 1 cm^2 polypropylene (plastic) and upholstery (cotton textile, similar the actual textile present in tram seats) surfaces resulting in final concentrations of ca. $10^{4–5}$ and $10^{6–7}$ $TCID_{50}/cm^2$, respectively. After allowing the suspension to dry for 30 min, samples were exposed to 100 ppm O_3 for up to 25 min in a Sanibox C900 equipment (Jeanologia S.L.) set at 25 ± 2 °C and 95% RH. Thereafter, viruses were recovered from the surface using 900 μL of Dulbecco's Modified Eagle Medium (DMEM) and 10-fold diluted in PBS to determine the $TCID_{50}/cm^2$.

2.2.5. Viral inactivation kinetics in field experiments

Similarly, MNV and PEDV were used as viral models to assess the viral inactivation kinetics adapting the ISO 21702:2019 as described previously. Briefly, 1 cm^2 polypropylene plastic surfaces were seeded with 10^6 $TCID_{50}/cm^2$ MNV or 10^3 $TCID_{50}/cm^2$ PEDV in a BSL-2 cabinet and then placed in two different locations inside the domains. In particular, medium- (position P2 in Fig. 9) and wide-range (position P4 in Fig. 9) distance from the inlet point of the disinfectant were assessed in underground wagon, and short- (position P1 in Fig. 9) and wide-range (position P4 in Fig. 9) distance from the inlet point were assessed in tramway wagon. Ozonization was carried out the SDA-200-50 experimental set-up (LIC–VARESER (Spain)). The treatment consisted of 120 s of ozone injection, 18 min of ozone activity without ventilation, and a final ozone removal by ventilation and catalytic destruction. During the disinfection treatment in underground wagons, the ozone concentration was 54.8 ppm on average, the temperature 30 ± 2 °C with 87% RH. Similarly, the ozone treatment in tramway wagons was conducted at 32 ± 2 °C and 84% RHr.

In all the experiments, control samples consisting of inoculated surfaces not exposed to disinfection treatment were included. The virucidal activity was determined by comparing the titer of infectious

viruses of treated and control samples. Each experimental condition was assayed in triplicate.

3. Results and discussion

3.1. Aerodynamics validation

The air velocity has been analysed in simulations at different planes, vertical and horizontal, for both coaches. Fig. 4 shows the velocity distribution calculated in steady state in the tram coach, the most complex configuration due to the distribution of their 44 seats. The air moves round and round through the coach with a turnover time of 42.47 s. It presented the highest air velocities in the pipe and at the entrance of the coach (Fig. 4). After the first area of seats, the air distribution was rapidly homogenized within the whole section (Fig. 5).

The highest values of the air velocity were calculated in the central part of the domain. The average value within the main corridor was in a range of 1–1.2 m/s. The air velocity was reduced to values between 0.5 and 0.2 m/s on the sides, where the windows and seats were located. The lowest values corresponded to areas with a greater number of seats. A more detailed fluid flow performance is shown in Fig. 6, whereas Table 2 shows the isovolumes calculated within the domain.

After the fan submodel calibration, the CFD steady state simulation results were validated experimentally using five directional anemometers inside the coach. The sensors were positioned at 5 sensitive points to capture the fluid flow performance (Fig. 7). The comparison shows good match between the results calculated and measured (Table 3) which demonstrates that CFD model reproduced the air flow trend correctly.

The slight deviations observed in Table 3 can be justified because of inlet and outlet were both defined at a medium height in the model, while the real position was slightly higher and lower, respectively (Fig. 8). This was modified for the best of the system set. In addition, the CFD model is completely stagnant while the real coach can have small leaks.

3.2. Ozone distribution validation

Once fluid dynamics was validated, a pulse of ozone was performed to calculate the concentration distribution inside the domain, analysing the consumption of ozone by decomposition and surface deposition. Transient simulations were run for 20 min. Six virtual monitor points were distributed along the coach to analyse the ozone concentration distribution during and after the pulse (Figs. 9–11).

Figs. 10 and 11 show the ozone concentration increasing rapidly during the pulse. In the first seconds of operation, the recirculation of ozone throughout the tram coach is well appreciated; the ozone achieved the initial point in 28 s. The different points show a progressive increase in concentration: P1, P2 and so on, reproducing the same trend with a slightly time span, due to the relative position given in flow direction. After 5 min, the ozone pulse ended, and the ozone concentration achieved concentration greater than 100 ppm. After the pulse, the ozone concentration inside the tram coach homogenizes in approximately 60 s. Then, the ozone concentration decayed from 100 ppm to 70 ppm in 15 min, which implies an ozone consumption rate of 2 ppm/min, due to the decomposition and deposition on surfaces. Experimental ozone concentration profiles are in good agreement with the prediction of the simulations. Fig. 12 shows the ozone concentration monitored in P3 (Fig. 9) at different relative humidity. As Eq. (5) predicts, the increase of

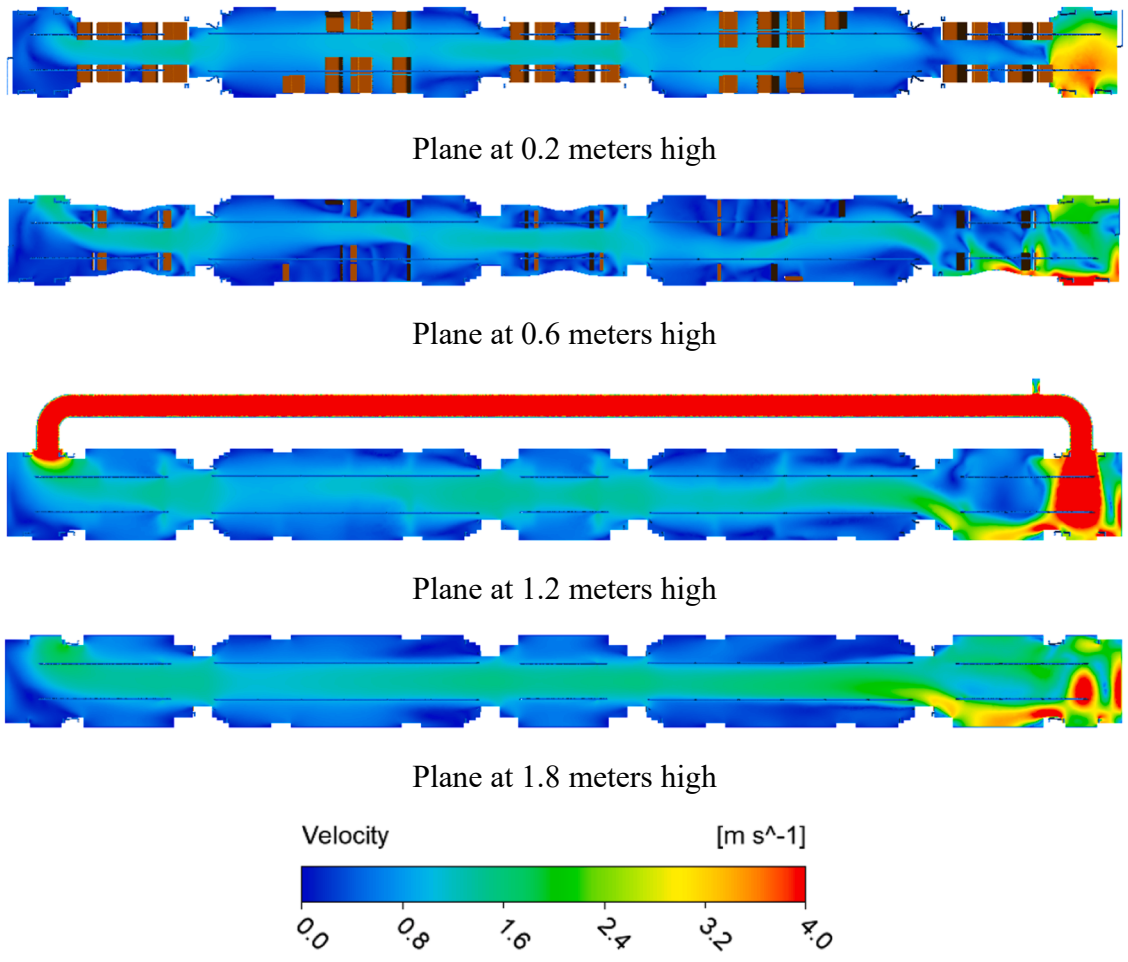

Fig. 4. Air velocity distribution at horizontal different planes.

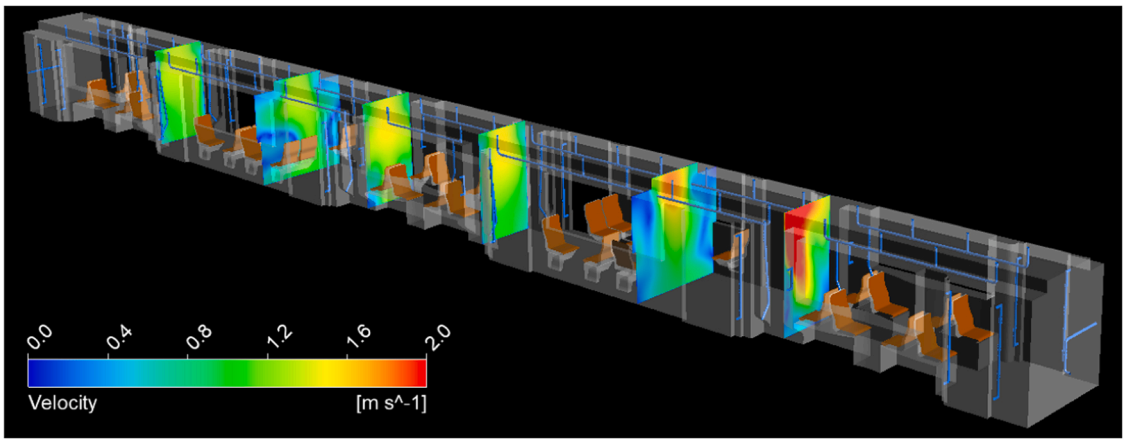

Fig. 5. Air velocity distribution in the perpendicular section to the main direction of the airflow.

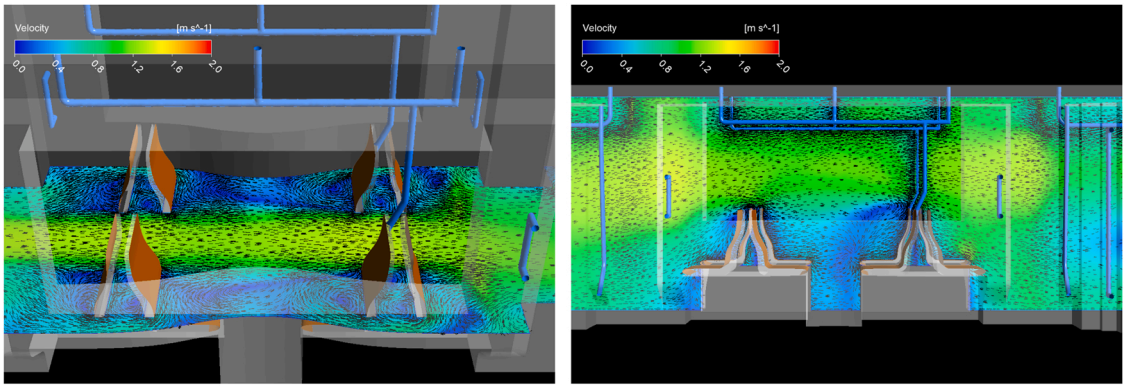

Fig. 6. Air velocity distribution in horizontal and vertical planes around the seats.

Table 2
Summary of air velocity distribution. The % volume is relative to the air volume in the coach.

Air velocity (m/s)	Location	Air volume (%)
Low (< 0.10)	Areas closest to surfaces where velocity tends to zero	17.3
Medium (0.10–0.20)	Changes of main section and seat shadows	8.0
High (> 0.20)	Main section/corridor	74.7

humidity will increases the ozone decomposition rate and then, the ozone saturation concentration at higher humidity conditions results in a lower steady state ozone concentration. Thus, to keep the same ozone concentration in high humidity conditions there is the need to increase

Table 3
Air velocity results measured vs calculated.

Point	Coordinates (X, Y, Z)	Position	Measured	Calculated
A1	(1, 0, 1.6)	Inlet	10.1 ± 0.4	11.4
A2	(10.3, 0.7, 1.15)	Lateral middle	0.9 ± 0.1	0.8
A3	(10.7, 1.35, 1.9)	Central top	1.1 ± 0.1	1.3
A4	(14, 1.15, 0.25)	Central bottom	0.8 ± 0.1	1.2
A5	(27.5, 0, 0.35)	Outlet	9.2 ± 0.1	9.2

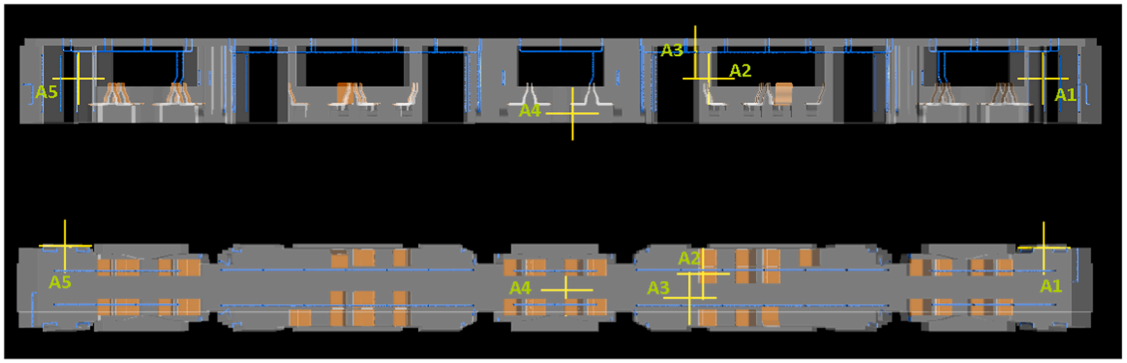

Fig. 7. Monitoring points (A1, A2, A3, A4 and A5).

Fig. 8. Anemometers in the tram coach: A1 (left), A2 and A3 (middle), and A5 (right).

the ozone-generator power. Fig. 12 shows the experimental results of the ozonation of the tram coach in two different days. As humidity in field experiment is not a variable to be controlled in-situ, the values of the magnitude are reported. The ozone concentration profiles show the same trend with independence of the experiment and their absolute value is interpreted according Eq. (5). After an initial transient due to injection procedure, the concentration reaches its steady state concentration after 5 min of the ozone injection and remains constant for 15 min (see Fig. 12). These times can be increased changing the injection protocols of the ozone generator.

The surfaces with the highest ozone consumption are those made up of synthetic materials and textile materials (seats). Thus, a consumption of 3.75 g and 2.36 g were calculated, respectively. In addition, 2.76 g of ozone was consumed due to the ozone decomposition. Both represented a total consumption of 8.87 g in 20 min, which represented a percentage of 29.6% of the total mass of ozone introduced, from which 68.9% is due to the surfaces deposition, and the 31.1% was due to decomposition. CFD ozone consumption results showed high dependence on the γ parameter selected. Fig. 13 shows a good homogenization of ozone in the 3D domain. The concentration gradients near the seat indicates they were the main sink of ozone, which guarantees that the ozone achieves all the surfaces.

3.3. Biological experiments validation

3.3.1. Viral inactivation kinetics at lab scale

In lab scale experiments, PEDV and MNV seeded onto polypropylene (plastic) and upholstery surfaces were significantly inactivated when exposed to 100 ppm O_3 for up to 25 min at 25 °C and 95% RH (Table 4). Non-enveloped (MNV) and enveloped (PEDV) viral models exposed to O_3 for extended exposure time showed a viral infectivity decrease that fits a negative exponential pattern (Fig. 14). Specifically, 99.89% and

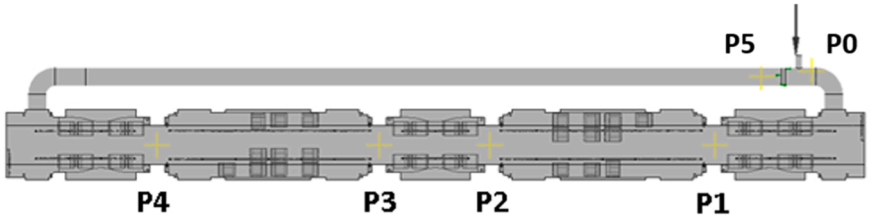

Fig. 9. Virtual monitor points to calculate the ozone concentration distribution.

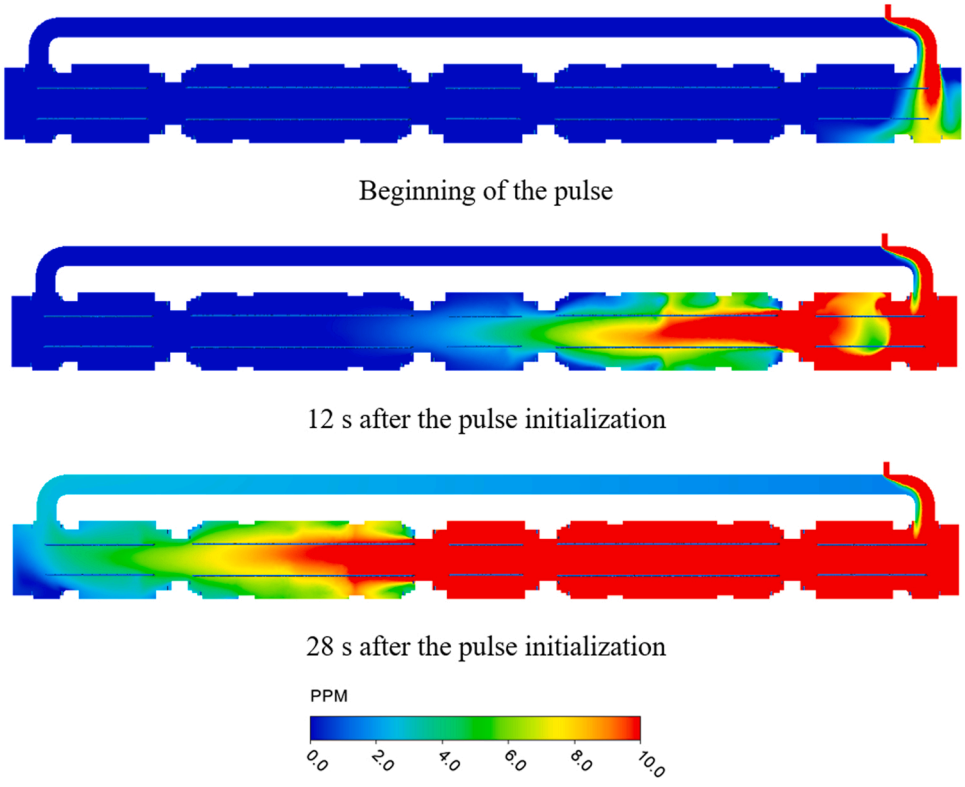

Fig. 10. Ozone concentration during the pulse performance.

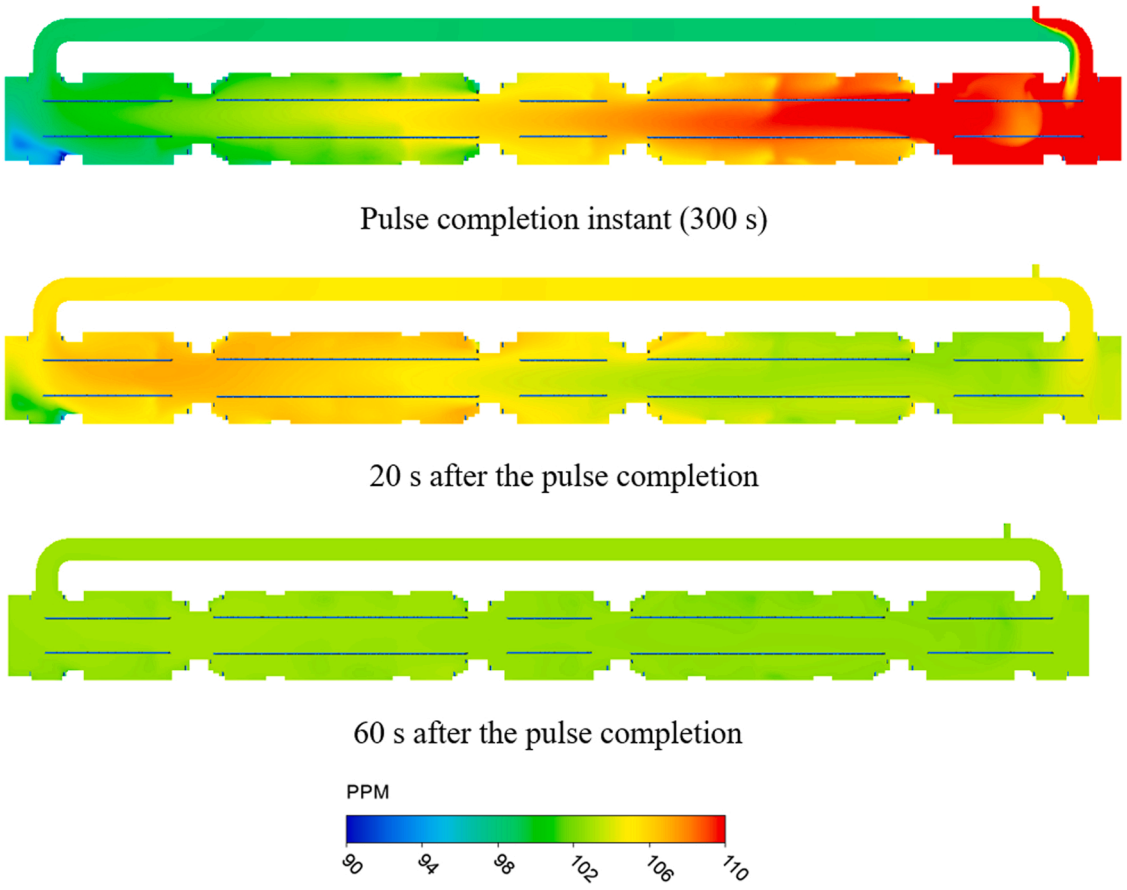

Fig. 11. Ozone concentration after the pulse completion.

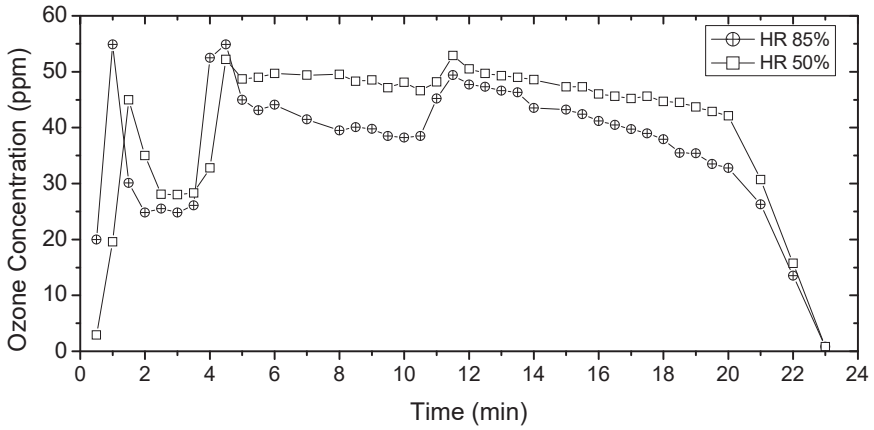

Fig. 12. Ozone concentration monitored in P3 (see Fig. 9) for different relative humidity. The humidity corresponds to the ambient value measured in the wagon the day of the experiment. For higher humidity, the steady state ozone concentration is lower as Eq. (5) predicts.

$>$ 99.79 of initial MNV and PEDV titers were inactivated after 25 min in plastic surfaces, resulting in a complete inactivation below the limit of detection of the method (1.15 log $TCID_{50}/cm^2$) in the latter case. Despite the similar titer reductions observed in both viral models, the higher MNV initial load (5.24 ± 0.19 log $TCID_{50}/cm^2$) compared to PEDV (3.83 ± 0.07 log $TCID_{50}/cm^2$) could explain the residual infectivity detected for the non-enveloped surrogate after 25 min of treatment. A similar infectivity reduction trend was observed for both viruses seeded upholstery compared to plastic surfaces. HCoV 229-E, another surrogate for SARS-CoV-2, inoculated on aluminum surfaces was not inactivated following an exposure to up to 0.6 ppm O_3 for 20 min at 60% RH in laboratory settings [4]. Unfortunately, we assessed a restricted range of exposure up to 10 min for upholstery samples, finally limiting a more comprehensive comparison between the viral inactivation kinetics in different surfaces.

3.3.2. *Viral inactivation kinetics on public transport coaches*

As the antiviral activity of ozone was demonstrated at the lab scale experiments, the following experiments were performed in underground and tram coaches. Results showed that significant reductions in infectivity were detected for both viral models following a 54.8 ppm O_3 exposure during 18 min at 87% RH (Tables 5 and 6). In detail, MNV was

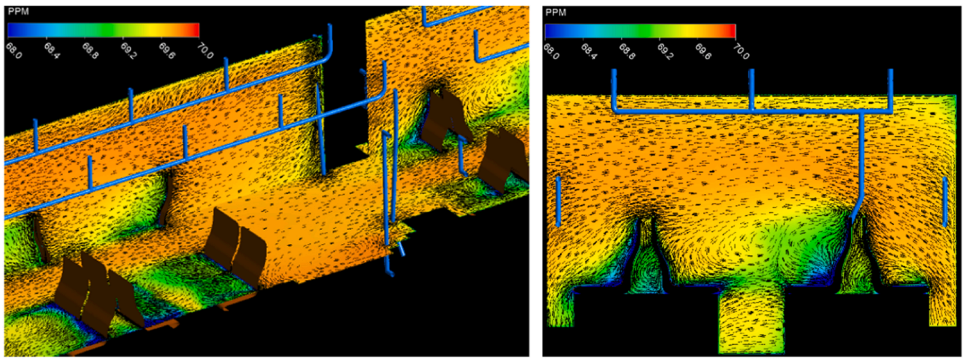

Fig. 13. Ozone concentration inside the domain.

Table 4
Kinetic effect of ozone on murine norovirus (MNV) and porcine epidemic diarrhea virus (PEDV) infectivity seeded on plastic and upholstery surfaces. Lab-scale tests were conducted at constant conditions of 100 ppm ozone and 95% relative humidity. Viral titers are indicated as log $TCID_{50}/cm^2$ and infectivity reductions as log reduction and percentage with respect to untreated control samples. Different letters indicate significant differences among treatments ($p < 0.05$).

Surface material	Exposure time (min)	MNV			PEDV		
		Titer (log $TCID_{50}/cm^2$)	Titer reduction (log)	Titer reduction (%)	Titer (log $TCID_{50}/cm^2$)	Titer reduction (log)	Titer reduction (%)
Plastic	Control	5.24 ± 0.19a			3.83 ± 0.07a		
	5	4.62 ± 0.38ab	0.62	76.01	3.37 ± 0.19b	0.46	65.33
	10	4.32 ± 0.32b	0.92	87.98	3.37 ± 0.07b	0.46	65.33
	15	3.49 ± 0.31c	1.75	98.22	< 1.15c	> 2.68	> 99.79
	25	2.28 ± 0.14d	2.96	99.89	< 1.15c	> 2.68	> 99.79
Upholstery	Control	5.87 ± 0.07a			3.37 ± 0.12a		
	5	5.24 ± 0.31ab	0.63	76.56	3.08 ± 0.07b	0.29	48.71
	10	4.91 ± 0.31b	0.96	89.04	2.83 ± 0.07c	0.54	71.16

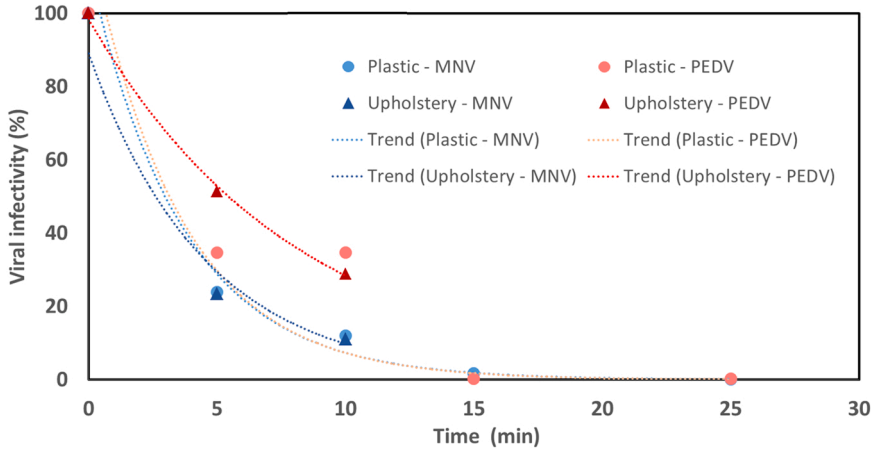

Fig. 14. Kinetic effect of ozone on murine norovirus (MNV) and porcine epidemic diarrhea virus (PEDV) infectivity seeded on plastic and upholstery surfaces. Points on the graph refer to observed values and lines indicate fitted first order inactivation kinetics.

Table 5
Disinfectant efficacy of ozone on murine norovirus (MNV) and porcine epidemic diarrhea virus (PEDV) infectivity seeded on plastic surfaces and tested in underground wagons at two distances from the inlet point. The average ozone concentration of 54.8 ppm was maintained during 18 min at 87% RH. Viral titers are indicated as log $TCID_{50}/cm^2$ and infectivity reductions as log and percentage with respect to untreated control samples. Different letters indicate significant differences among treatments ($p < 0.05$).

Sample	MNV			PEDV		
	Titer (log $TCID_{50}/cm^2$)	Titer reduction (log)	Titer reduction (%)	Titer (log $TCID_{50}/cm^2$)	Titer reduction (log)	Titer reduction (%)
Control	6.87 ± 0.14a			5.54 ± 0.07a		
Medium-range	4.57 ± 0.43b	2.29	99.46	< 1.15c	> 3.39	> 99.96
Wide-range	3.66 ± 0.07c	3.21	99.95	1.73 ± 0.15b	2.81	99.79

Table 6
Disinfectant efficacy of ozone on murine norovirus (MNV) and porcine epidemic diarrhea virus (PEDV) infectivity seeded on plastic surfaces and tested in tramway wagons at two distances from the inlet point. Disinfection treatments consisted of 54.8 ppm ozone during 18 min at 84% RH. Viral titers are indicated as log $TCID_{50}/cm^2$ and infectivity reductions as percentages with respect to control sample. Different letters indicate significant differences among treatments ($p > 0.05$).

Disinfectant	MNV			PEDV		
	Titer (log $TCID_{50}/cm^2$)	Titer reduction (log)	Titer reduction (%)	Titer (log $TCID_{50}/cm^2$)	Titer reduction (log)	Titer reduction (%)
Control	7.01 ± 0.09a			3.62 ± 0.00a		
Close-range	4.95 ± 0.22b	2.06	98.56	< 1.15b	> 2.47	> 96.25
Wide-range	4.87 ± 0.19bc	2.14	98.82	< 1.15b	> 2.47	> 96.25

inactivated by 2.06–3.21 log $TCID_{50}/cm^2$ resulting in 98.56–99.95% reductions with variations depending on the distance from the O_3 inlet point in both types of coaches tested. Intriguingly, a higher MNV reduction was detected in surfaces placed at wide (3.21 log $TCID_{50}/cm^2$) (P4 on Fig. 9) than medium (2.29 log $TCID_{50}/cm^2$) (P2 on Fig. 9) distances from the inlet point of the disinfectant. The distribution of ozone concentration during the pulse performance as explained in Section 3.2 contributes to explain these results. PEDV showed titer reductions of 2.47 to > 3.39 log $TCID_{50}/cm^2$ accounting for 96.25 to > 99.96% reduction with respect to the untreated controls. Interestingly, PEDV showed complete inactivation (residual infectivity below < 1.15 log $TCID_{50}/cm^2$, the detection limit of the assay) in all tested conditions with the only exception of the surfaces placed at a wide-range distance (P4) from the O_3 inlet point. Again, the lower PEDV initial titer compared to MNV could partially explain the complete inactivation as well the residual infectivity at a wide-range distance observed for the enveloped model. Statistical significant differences with respect to the location of the sample were observed for MNV and PEDV tested in underground but not in tram coaches.

Comparing bacteriophages, the dosage of 114 ppm O_3/min at 55% RH has been suggested as effective dosage against the non-enveloped dsDNA T7 phage, thus disinfecting at a conservatively high dose compared to 30 ppm/min required to inactivate the enveloped dsRNA Φ6 phage that is theoretically most similar to SARS-CoV-2 [53]. A previous study reported that 30–300 ppm O_3/min for 20–30 min as the dosage required to inactivate 99% of twelve different viruses, representing DNA and RNA viruses with and without envelope, on plastic, glass, and stainless steel surfaces at 45% RH [15]. This data suggests that a dose of 300 ppm O_3/min for a 30 min treatment would effectively inactivate 99% of a wide range of viruses tested on a variety of solid substrate surfaces. Overall, our laboratory and field tests results resemble those inactivation kinetics as > 99% inactivation rates were achieved following treatments either of 100 ppm for 15–25 min or 54.8 ppm O_3 for 18 min at 84–87% RH.

Beside the different surrogates employed as models for SARS-CoV-2 in previous studies, viral inactivation is undoubtedly dose-dependent. However, for application purposes it is notably to underline that relative humidity plays a key role in enhancing O_3 mediated inactivation, as the higher RH the more virus is inactivated (data not shown, [15,18]). Thus, specific assays are needed to bring to light how and at which extent RH affects the viral inactivation rates in field tests.

4. Conclusions

The results shown in this work conclude that the ozone is an effective disinfectant for viruses in moderated concentration and application times in real transportation systems. The disinfection procedure must be done in cycles with the tram coach unoccupied because the ozone concentration is high enough to produce health issues in humans, alternating the ozone injection with the catalytic decomposition of the residual ozone. The application time must be fixed to guarantee the proper disinfection level together a lower ozonization of the indoor materials.

Although the ozone is not recognized by the ECHA as a biocidal product by the current regulations of the EU in the Biocidal Product Regulation (BPR), it is allowed its utilization by the transitional Article 93 for *in-situ* generated biocides. That allows the utilization of the ozone as disinfectant and virucidal product when it is produced by corona discharge generators. In this work the effectiveness of the ozone against coronavirus and norovirus surrogates confirm the viability of the ozonization as a valid disinfection procedure against the SARS-CoV-2 and human enteric viruses. Although the role of environment-to-human COVID-19 spread remains under debate, fomites are significantly taking part in the transmission of human enteric viruses [54]. Results from this study clearly supports the use of ozone as an efficient measure for virus inactivation in public transport. In lab scale experiments, MNV and PEDV inactivation is reached for ozone concentrations of 100 ppm for 25 min at 25 °C and 95% RH. In field experiments, the same inactivation efficiency has attained with 55 ppm of ozone for 20 min at 32 °C and 87% RH showing the relevance of humidity on the inactivation efficiency. In conclusion, our results are of interest to tune disinfection treatments of public transport vehicles aimed to prevent and control the spread of SARS-CoV-2 and human enteric viruses through contaminated surfaces.

CRediT authorship contribution statement

Irene Falcó: Investigation, Data curation. **Walter Randazzo**: Methodology, Investigation, Writing manuscript, Reviewing. **Gloria Sánchez**: Methodology, Analysis, Supervision. **Jose Vilarroig**: Software, Investigation. **Javier Climent**: Software, Methodology, Investigation, Writing manuscript, Reviewing, **Sergio Chiva**: Methodology, Analysis, Supervision. **Antonio Chica**: Conceptualization, Analysis, Project Supervision: **Javier Navarro-Laboulais**: Software, Methodology, Analysis, Writing manuscript, Reviewing.

Declaration of Competing Interest

The authors declare that they have no known competing financial interests or personal relationships that could have appeared to influence the work reported in this paper.

Acknowledgments

The authors thanks to the companies LIC – Levantina Ingenieria y Construcción S.L. (Spain) and Vareser (Spain) for funding this study. The authors also acknowledge FGV-Ferrocarriles de la Generalitat Valenciana to supply the tram coach to carry out the field experiments. Especial thanks to José Ruz and José Barbeta to supply us the field experimental data.

Appendix A. Supplementary material

Supplementary data associated with this article can be found in the online version at doi:10.1016/j.jece.2021.106217.

References

[1] M. Klompas, M.A. Baker, C. Rhee, Airborne transmission of SARS-CoV-2: theoretical considerations and available evidence, JAMA 324 (2020) 441–442, https://doi.org/10.1001/jama.2020.12458.

[2] V. Stadnytskyi, C.E. Bax, A. Bax, P. Anfinrud, The airborne lifetime of small speech droplets and their potential importance in SARS-CoV-2 transmission, Proc. Natl. Acad. Sci. USA 117 (2020) 11875–11877, https://doi.org/10.1073/pnas.2006874117.

[3] J.S. Abrahão, L. Sacchetto, I.M. Rezende, R.A.L. Rodrigues, A.P.C. Crispim, C. Moura, D.C. Mendonça, E. Reis, F. Souza, G.F.G. Oliveira, I. Domingos, P.V. de Miranda Boratto, P.H.B. Silva, V.F. Queiroz, T.B. Machado, L.A.F. Andrade, K. L. Lourenço, T. Silva, G.P. Oliveira, V. de Souza Alves, P.A. Alves, E.G. Kroon, G. de Souza Trindade, B.P. Drumond, Detection of SARS-CoV-2 RNA on public surfaces in a densely populated urban area of Brazil: a potential tool for monitoring the circulation of infected patients, Sci. Total Environ. 766 (2021), 142645, https://doi.org/10.1016/j.scitotenv.2020.142645.

[4] T. Moreno, R.M. Pintó, A. Bosch, N. Moreno, A. Alastuey, M.C. Minguillón, E. Anfruns-Estrada, S. Guix, C. Fuentes, G. Buonanno, L. Stabile, L. Morawska, X. Querol, Tracing surface and airborne SARS-CoV-2 RNA inside public buses and subway trains, Environ. Int. 147 (2021), 106326, https://doi.org/10.1016/j.envint.2020.106326.

[5] T. Greenhalgh, J.L. Jimenez, K.A. Prather, Z. Tufekci, D. Fisman, R. Schooley, Ten scientific reasons in support of airborne transmission of SARS-CoV-2, Lancet 397 (2021) 1603–1605, https://doi.org/10.1016/S0140-6736(21)00869-2.

[6] G. Kampf, D. Todt, S. Pfaender, E. Steinmann, Persistence of coronaviruses on inanimate surfaces and their inactivation with biocidal agents, J. Hosp. Infect. 104 (2020) 246–251, https://doi.org/10.1016/j.jhin.2020.01.022.

[7] N. van Doremalen, T. Bushmaker, D.H. Morris, M.G. Holbrook, A. Gamble, B. N. Williamson, A. Tamin, J.L. Harcourt, N.J. Thornburg, S.I. Gerber, J.O. Lloyd-Smith, E. de Wit, V.J. Munster, Aerosol and surface stability of SARS-CoV-2 as compared with SARS-CoV-1, N. Engl. J. Med. 382 (2020) 1564–1567, https://doi.org/10.1056/NEJMc2004973.

[8] K.R. Wigginton, T. Kohn, Virus disinfection mechanisms: the role of virus composition, structure, and function, Curr. Opin. Virol. 2 (2012) 84–89, https://doi.org/10.1016/j.coviro.2011.11.003.

[9] R. Broer, B. Boson, W. Spaan, F.-L. Cosset, J. Corver, Important role for the transmembrane domain of severe acute respiratory syndrome coronavirus spike protein during entry, J. Virol. 80 (2006) 1302–1310, https://doi.org/10.1128/JVI.80.3.1302-1310.2006.

[10] L.A. Lopez, A.J. Riffle, S.L. Pike, D. Gardner, B.G. Hogue, Importance of conserved cysteine residues in the coronavirus envelope protein, J. Virol. 82 (2008) 3000–3010, https://doi.org/10.1128/JVI.01914-07.

[11] R.J. Rowen, Ozone and oxidation therapies as a solution to the emerging crisis in infectious disease management: a review of current knowledge and experience, Med. Gas Res. 9 (2019) 232–237, https://doi.org/10.4103/2045-9912.273962.

[12] D. Schoeman, B.C. Fielding, Coronavirus envelope protein: current knowledge, Virol. J. 16 (2019) 69, https://doi.org/10.1186/s12985-019-1182-0.

[13] B.L. Loeb, C.M. Thompson, J. Drago, H. Takahara, S. Baig, Worldwide ozone capacity for treatment of drinking water and wastewater: a review, Ozone Sci. Eng. 34 (2012) 64–77, https://doi.org/10.1080/01919512.2012.640251.

[14] C. Morrison, A. Atkinson, A. Zamyadi, F. Kibuye, M. McKie, S. Hogard, P. Mollica, S. Jasim, E.C. Wert, Critical review and research needs of ozone applications related to virus inactivation: potential implications for SARS-CoV-2, Ozone Sci. Eng. 43 (2021) 2–20, https://doi.org/10.1080/01919512.2020.1839739.

[15] J.B. Hudson, M. Sharma, S. Vimalanathan, Development of a practical method for using ozone gas as a virus decontaminating agent, Ozone Sci. Eng. 31 (2009) 216–223, https://doi.org/10.1080/01919510902747969.

[16] J. Zhang, C. Zheng, X. Geng-fu, Z. Yuan-Quan, G. Rong, Examination of the efficacy of ozone solution disinfectant in in activating SARS virus, Chin. J. Disinfect. (2004). /paper/EXAMINATION-OF-THE-EFFICACY-OF-OZONE-SOLUTION-IN-IN-Rong/66d233f521a4cb2fd442c16edeec1787f52339e9 (Accessed 13 May 2021).

[17] C. Tizaoui, Ozone: a potential oxidant for COVID-19 virus (SARS-CoV-2), Ozone Sci. Eng. 42 (2020) 378–385, https://doi.org/10.1080/01919512.2020.1795614.

[18] B. Bayarri, A. Cruz-Alcalde, N. López-Vinent, M.M. Micó, C. Sans, Can ozone inactivate SARS-CoV-2? A review of mechanisms and performance on viruses, J. Hazard. Mater. 415 (2021), 125658, https://doi.org/10.1016/j.jhazmat.2021.125658.

[19] J. Ferre-Aracil, S.C. Cardona, J. Navarro-Laboulais, Determination and validation of Henry's constant for ozone in phosphate buffers using different analytical methodologies, Ozone Sci. Eng. (2014).

[20] World Health Organization. Air Quality Guidelines for Europe, 2nd ed., World Health Organization, Regional Office for Europe, Copenhagen, 2000.

[21] D.N. Sørensen, C.J. Weschler, Modeling-gas phase reactions in indoor environments using computational fluid dynamics, Atmos. Environ. 36 (2002) 9–18, https://doi.org/10.1016/S1352-2310(01)00479-4.

[22] J. Russo, H.E. Khalifa, CFD analysis of personal ventilation with volumetric chemical reactions, HVACR Res. 16 (2010) 799–812, https://doi.org/10.1080/10789669.2010.10390935.

[23] J. Shen, Z. Gao, Ozone removal on building material surface: a literature review, Build. Environ. 134 (2018) 205–217, https://doi.org/10.1016/j.buildenv.2018.02.046.

[24] C.J. Weschler, Ozone in indoor environments: concentration and chemistry: ozone in indoor environments, Indoor Air 10 (2000) 269–288, https://doi.org/10.1034/j.1600-0668.2000.010004269.x.

[25] G. Tamas, C. Weschler, Z. Bakobiro, D. Wyon, P. Stromtejsen, Factors affecting ozone removal rates in a simulated aircraft cabin environment, Atmos. Environ. 40 (2006) 6122–6133, https://doi.org/10.1016/j.atmosenv.2006.05.034.

[26] C.J. Weschler, Ozone's impact on public health: contributions from indoor exposures to ozone and products of ozone-initiated chemistry, Environ. Health Perspect. 114 (2006) 1489–1496, https://doi.org/10.1289/ehp.9256.

[27] B.K. Coleman, H. Destaillats, A.T. Hodgson, W.W. Nazaroff, Ozone consumption and volatile byproduct formation from surface reactions with aircraft cabin materials and clothing fabrics, Atmos. Environ. 42 (2008) 642–654, https://doi.org/10.1016/j.atmosenv.2007.10.001.

[28] M. Kruza, A.C. Lewis, G.C. Morrison, N. Carslaw, Impact of surface ozone interactions on indoor air chemistry: a modeling study, Indoor Air 27 (2017) 1001–1011, https://doi.org/10.1111/ina.12381.

[29] S.D. Richardson, A.D. Thruston, T.V. Caughran, P.H. Chen, T.W. Collette, T. L. Floyd, K.M. Schenck, B.W. Lykins, G. Sun, G. Majetich, Identification of new ozone disinfection byproducts in drinking water, Environ. Sci. Technol. 33 (1999) 3368–3377, https://doi.org/10.1021/es981218c.

[30] A. Arthur, B. Sidney, Mechanism of gas phase decomposition of ozone, Therm. Photochem. React. (1959), https://doi.org/10.1021/ba-1959-0021.ch052.

[31] S. Benson, A. Axworthy, Mechanism of the gas phase, thermal decomposition of ozone, J. Chem. Phys. 26 (1957) 1718–1726, https://doi.org/10.1063/1.1743610.

[32] S. Benson, A. Axworthy, Reconsideration of the rate constants from the thermal decomposition of ozone, J. Chem. Phys. 42 (1965) 2614–2615, https://doi.org/10.1063/1.1696345.

[33] J.D. McClurkin, D.E. Maier, Half-life time of ozone as a function of air conditions and movement, Julius-Kühn-Archiv 425 (2010) 381–385, https://doi.org/10.5073/JKA.2010.425.167.326.

[34] J.D. McClurkin, D.E. Maier, K.E. Ileleji, Half-life time of ozone as a function of air movement and conditions in a sealed container, J. Stored Prod. Res. 55 (2013) 41–47, https://doi.org/10.1016/j.jspr.2013.07.006.

[35] B. Dhandapani, S.T. Oyama, Gas phase ozone decomposition catalysts, Appl. Catal. B Environ. 11 (1997) 129–166, https://doi.org/10.1016/S0926-3373(96)00044-6.

[36] P.M. Álvarez, F.J. Masa, J. Jaramillo, F.J. Beltrán, V. Gómez-Serrano, Kinetics of ozone decomposition by granular activated carbon, Ind. Eng. Chem. Res. 47 (2008) 2545–2553, https://doi.org/10.1021/ie071360z.

[37] H. Valdés, M. Sánchez-Polo, J. Rivera-Utrilla, C.A. Zaror, Effect of ozone treatment on surface properties of activated carbon, Langmuir 18 (2002) 2111–2116, https://doi.org/10.1021/la010920a.

[38] C.S. Conover, Transmission of severe acute respiratory syndrome coronavirus 2 via contaminated surfaces: what is to be done? Clin. Infect. Dis. (2020), ciaa1586 https://doi.org/10.1093/cid/ciaa1586.

[39] H. Kanamori, D.J. Weber, W.A. Rutala, Role of the healthcare surface environment in severe acute respiratory syndrome coronavirus 2 (SARS-CoV-2) transmission and potential control measures, Clin. Infect. Dis. (2020), ciaa1467, https://doi.org/10.1093/cid/ciaa1467.

[40] K.A. Reynolds, J.D. Sexton, F. Garavito, B. Anderson, J.M. Ivaska, Impact of a whole-room atomizing disinfection system on healthcare surface contamination, pathogen transfer, and labor efficiency, Crit. Care Explor. 3 (2021) 0340, https://doi.org/10.1097/CCE.0000000000000340.

[41] ANSYS® Academic Research, Release 19.2, Help System, ANSYS CFX Reference Guide, ANSYS Inc. 2019. ⟨https://www.ansys.com/academic/terms-and-conditions⟩.

[42] F.R. Menter, Two-equation eddy-viscosity turbulence models for engineering applications, AIAA J. 32 (1994) 1598–1605, https://doi.org/10.2514/3.12149.

[43] S.S. Parmar, D. Grosjean, Laboratory tests of KI and alkaline annular denuders, Atmos. Environ. Part A Gen. Top. 24 (1990) 2695–2698, https://doi.org/10.1016/0960-1686(90)90150-L.

[44] J.I. Steinfeld, S.M. Adler-Golden, J.W. Gallagher, Critical survey of data on the spectroscopy and kinetics of ozone in the mesosphere and thermosphere, J. Phys. Chem. Ref. Data 16 (1987) 911–951, https://doi.org/10.1063/1.555796.

[45] JPL Data Evaluation, (n.d.). ⟨https://jpldataeval.jpl.nasa.gov/⟩. (Accessed 11 April 2021).

[46] IUPAC Task Group on Atmospheric Chemical Kinetic Data Evaluation, (n.d.). ⟨http://iupac-dev.ipsl.jussieu.fr/⟩. (Accessed 11 April 2021).

[47] NIST Chemical Kinetics Database, (n.d.). ⟨https://kinetics.nist.gov/kinetics/⟩. (Accessed 11 April 2021).

[48] W.P.L. Carter, A detailed mechanism for the gas-phase atmospheric reactions of organic compounds, Atmos. Environ. Part A Gen. Top. 24 (1990) 481–518, https://doi.org/10.1016/0960-1686(90)90005-8.

[49] V. Damian, A. Sandu, M. Damian, F. Potra, G.R. Carmichael, The kinetic preprocessor KPP-a software environment for solving chemical kinetics, Comput. Chem. Eng. 26 (2002) 1567–1579, https://doi.org/10.1016/S0098-1354(02)00128-X.

[50] A. Sandu, R. Sander, Technical note: simulating chemical systems in Fortran90 and Matlab with the kinetic preprocessor KPP-2.1, Atmos. Chem. Phys. 6 (2006) 187–195, https://doi.org/10.5194/acp-6-187-2006.

[51] A.L. Buck, New equations for computing vapor pressure and enhancement factor, J. Appl. Meteorol. Climatol. 20 (1981) 1527–1532, https://doi.org/10.1175/1520-0450(1981)020<1527:NEFCVP>2.0.CO;2.

[52] H. Puente, W. Randazzo, I. Falcó, A. Carvajal, G. Sánchez, Rapid selective detection of potentially infectious porcine epidemic diarrhea coronavirus exposed to heat treatments using viability RT-qPCR, Front. Microbiol. 11 (2020) 1911, https://doi.org/10.3389/fmicb.2020.01911.

[53] C. Tseng, C. Li, Inactivation of surface viruses by gaseous ozone, J. Environ. Health 70 (2008) 56–62.

[54] S.A. Boone, C.P. Gerba, Significance of fomites in the spread of respiratory and enteric viral disease, Appl. Environ. Microbiol. 73 (2007) 1687–1696, https://doi.org/10.1128/AEM.02051-06.